ARTICLES
PUBLISHED ONLINE: 3 NOVEMBER 2013 | DOI: 10.1038/NMAT3784
nature materials

Origin of additional capacities in metal oxide lithium-ion battery electrodes

Yan-Yan Hu[1], Zigeng Liu[1], Kyung-Wan Nam[2], Olaf J. Borkiewicz[3], Jun Cheng[1], Xiao Hua[1], Matthew T. Dunstan[1], Xiqian Yu[2], Kamila M. Wiaderek[3], Lin-Shu Du[4], Karena W. Chapman[3], Peter J. Chupas[3], Xiao-Qing Yang[2] and Clare P. Grey[1,4]*

Metal fluorides/oxides (MF_x/M_xO_y) are promising electrodes for lithium-ion batteries that operate through conversion reactions. These reactions are associated with much higher energy densities than intercalation reactions. The fluorides/oxides also exhibit additional reversible capacity beyond their theoretical capacity through mechanisms that are still poorly understood, in part owing to the difficulty in characterizing structure at the nanoscale, particularly at buried interfaces. This study employs high-resolution multinuclear/multidimensional solid-state NMR techniques, with *in situ* synchrotron-based techniques, to study the prototype conversion material RuO_2. The experiments, together with theoretical calculations, show that a major contribution to the extra capacity in this system is due to the generation of LiOH and its subsequent reversible reaction with Li to form Li_2O and LiH. The research demonstrates a protocol for studying the structure and spatial proximities of nanostructures formed in this system, including the amorphous solid electrolyte interphase that grows on battery electrodes.

Until a decade ago, the most viable choices for lithium-ion battery electrode materials were generally considered to be insertion materials, these materials reversibly accommodating lithium ions in 'host' sites in the lattice. The discovery that a series of metal salts (typically oxides and fluorides, MF_x and M_xO_y) could reversibly react with lithium through a conversion-type reaction where the metal salt is lithiated to form a composite structure comprising metal particles embedded in a lithium salt, $MF_x + xLi^+ + xe^- = M^0 + xLiF$ or $M_xO_y + 2yLi^+ + 2ye^- = xM^0 + yLi_2O$, potentially opens up approaches for exploiting multiple-electron transfers per redox centre[1–9]. These materials exhibit much higher specific energies as compared with present commercial lithium-ion battery insertion electrodes, such as $LiCoO_2$, $LiFePO_4$, $LiMn_2O_4$ and graphite. An intriguing aspect in the reaction of these systems, which has provoked much debate, is the additional reversible capacity shown beyond the theoretical capacity estimated on the basis the reduction of the metal cation to M^0 (ref. 9). This additional capacity was first reported for nanosized particles of the perovskite $SnMn_3C$, which showed, in contrast to micron-sized particles of this material, a reversible capacity of $\sim$150 mAh g^{-1} (ref. 10). The phenomenon is not unique to $SnMn_3C$, occurring more generally in most studied conversion materials. In 2002, this phenomenon was studied in M_xO_y/Li cells[11] by using transmission electron microscopy, and a 'polymer/gel-like film' was observed to form at the grain boundaries between nanoparticles at low voltages (1.9–0.0 V). The extra capacity was maintained for more that 800 cycles[11]. In contrast, it was argued on the basis of investigations first on RuO_2 (ref. 4) and then more generally on a range of fluorides and oxides[6,7,12–14] that a source of the additional capacity lies in the formation of a so-called space charge layer comprising Li^+ ions at the interface between the metal and lithium salt particles, charge compensated by additional electrons on the metal surface. These findings have spurred many discussions over the past 10 years[12,14–16], because of the intriguing possibility that the mechanism provides a more general approach for storing charge. At the heart of the debate lies the experimental difficulty in identifying the structures present at the buried metal/salt interfaces.

Here, we use a variety of short- and long-range structural characterization techniques to investigate the mechanism for charge storage in the prototype conversion reaction involving RuO_2. This material is chosen because it shows among the highest Coulombic efficiencies and good mass transport properties compared with other metal oxides/fluorides, and it does not form superparamagnetic nanoparticles (unlike the Fe and Co systems), allowing high-resolution NMR spectra to be obtained. We first use *in situ* synchrotron-based techniques to follow the short- and long-range electronic structural changes and monitor the fate of the RuO_2 in real time. ^{6}Li, ^{17}O and ^{1}H multi-dimensional solid-state NMR methods are then used to confirm short-range structure and more importantly to track the formation and the reaction of different chemical species at the grain boundaries, and furthermore, to investigate the mechanism for generating the additional capacity in this system. The experimental results, in combination with relevant theoretical calculations, show that a major source of the additional capacity in RuO_2 arises from the reversible reaction of LiOH to form LiH and solid electrolyte interphase (SEI) formation. The results have implications for the understanding of interfacial storage mechanisms in a wider range of nanocomposites as well as providing NMR strategies for characterizing the nature of the SEI that grows on essentially all electrode materials on cycling[17–19].

Results and discussion

Electrochemistry of the RuO_2/Li battery system. Figure 1a shows the electrochemical profile of a RuO_2/Li battery cycled with a rate of $C/30$ (the full capacity of the battery is accessed on a

[1]Department of Chemistry, University of Cambridge, Lensfield Road, Cambridge CB2 1EW, UK, [2]Chemistry Department, Brookhaven National Laboratory, New York 11973, USA, [3]X-ray Science Division, Advanced Photon Source, Argonne National Laboratory, Illinois 60439, USA, [4]Department of Chemistry, Stony Brook University, New York 11794-3400, USA. *e-mail: cpg27@cam.ac.uk

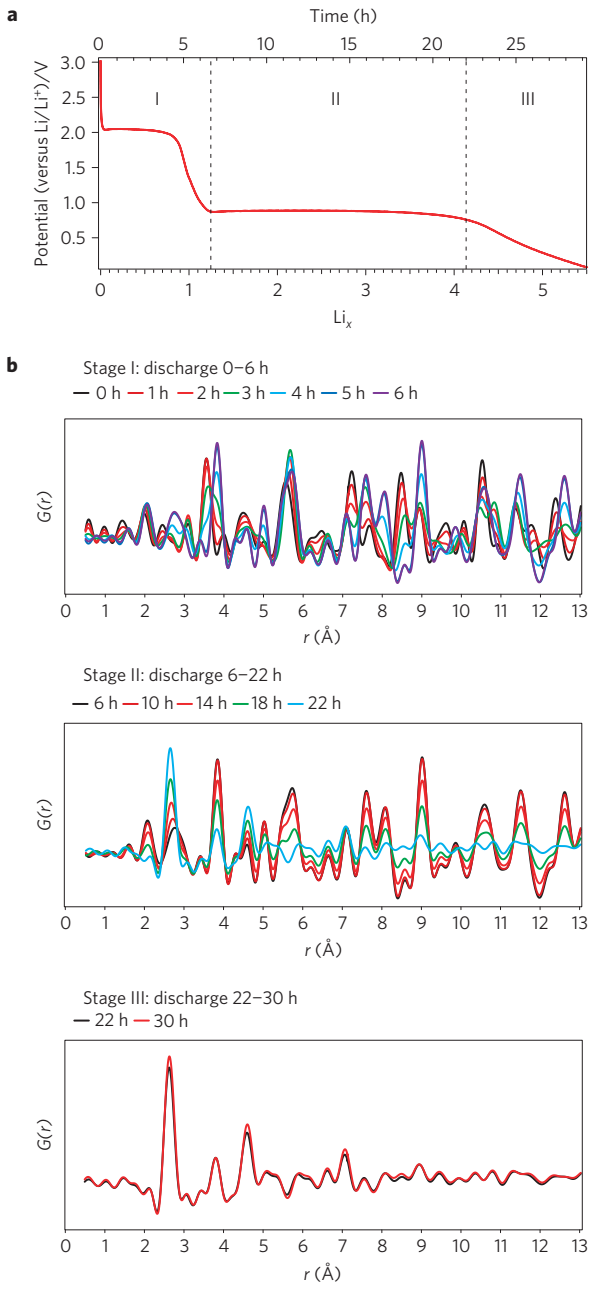

Figure 1 | *In situ* PDF analyses of the RuO_2/Li system reveal the changes in phase composition following battery discharge. a, The electrochemistry profile of a RuO_2/Li battery cycled at a rate of C/30. **b**, The *in situ* PDF patterns obtained from a RuO_2/Li battery. The PDF patterns are divided into three sets marked I, II and III, which are analogous to those marked on the electrochemical profile in **a**. The running time index (hour) is noted on top of each pattern set with lines of the same colour as those of the corresponding PDF patterns.

timescale of 30 h, assuming insertion of 5.6 Li per Ru atom, that is, including additional capacity beyond a four-electron process)[4]. The first process at 2.1 V and the subsequent sloping voltage profile (from 2.1 to 0.8 V) is generally assigned to Li intercalation into tetragonal RuO_2 to form an intermediate (tetragonal, metastable) phase Li_xRuO_2, and its further lithiation to form $LiRuO_2$ (ref. 20). The intermediate phase is thought to buffer the size mismatch between the tetragonal RuO_2 and orthorhombic $LiRuO_2$ lattices[20]. More recent work has shown that the three phases coexist during the 2.1 V 'plateau', both the range over which the phases exist and the extent of solid solution within these phases depending strongly on the RuO_2 particle size[21]. The evolution of these three RuO_2-based phases in the present system is not the main focus of this manuscript but is discussed in some detail in the Supplementary Information. The following plateau at 0.8 V is due to the conversion reaction from $LiRuO_2$ to Li_2O and Ru^0. Finally a continuous voltage drop is observed from 0.8 V until the end of discharge at 0.05 V, which has been ascribed to the 'interfacial insertion (or space charge)' region[12].

Real-time detection of the Ru-containing phases. *In situ* pair distribution function (PDF) methods and X-ray absorption spectroscopy (XAS) have been applied to monitor changes in Ru phase distribution, local structure and oxidation state during electrochemical cycling. The change in the *in situ* total scattering (diffraction) X-ray patterns (Supplementary Fig. 1b), from which the PDFs were derived, confirms that RuO_2 transforms to $LiRuO_2$ through the intermediate tetragonal phase Li_xRuO_2, and then from $LiRuO_2$ to Ru metal on lithiation, where x in this system is estimated to be between 0.2 and 0.5, the large error arising primarily from the additional capacity from SEI formation (see Supplementary Information). The real-space local structural information in the corresponding PDF data provides insight into the structure and phase evolution of the Ru components that is largely independent of the sample crystallinity, disorder or particle size, and is particularly useful for analysing the nanosized components in this system. Inspection of the PDF obtained *in situ* suggests three distinct stages (Fig. 1b). The variations in the abundance of the different Ru phases during these stages were evaluated by monitoring the integrated intensity of specific peaks in the PDFs corresponding to atom–atom distances characteristic of each phase and phase fractions were extracted from refinements (Supplementary Fig. 2e). In stage I (0 Li → 1.3Li), characteristic correlations of the RuO_2 phase (for example, the Ru^{IV}–Ru^{IV} peaks at 3.6 Å) gradually decrease with the increase of the $LiRuO_2$ correlations (Ru^{III}–Ru^{III} peaks at 2.8 and 3.8 Å) tracking the insertion of Li into the $Ru^{IV}O_2$ structure. (Note that we cannot distinguish between Li_xRuO_2 and RuO_2 with this analysis method.) In stage II (approximately 1.3 Li → 4.2 Li), the Ru^{III}–O peaks at approximately 2.0 Å slowly disappear as $LiRuO_2$ converts to Ru nanoparticles of average diameter 13 Å. In stage III (approximately 4.2 Li to 5.6 Li), the PDFs remain relatively unchanged with no significant variation in the Ru nanoparticle structure, size or abundance. Phase fractions extracted from refinements during all three stages of the *in situ* PDF data are presented in the Supplementary Information.

The Ru oxidation state and structural changes are observed, respectively, in the X-ray absorption near-edge structure (XANES) and extended X-ray absorption fine-structure (EXAFS) spectroscopies. The *in situ* data can again be divided into three stages (Fig. 2). During stage I (0–1.3 Li), the insertion of lithium into the RuO_2 structure is manifested by a gradual shift to the lower energy of the absorption edge in the XANES spectra, indicating the reduction of ruthenium. The EXAFS data were analysed by fitting the EXAFS spectra (Fig. 2a,b) yielding bond lengths consistent with those extracted from the PDF patterns. Again, the reaction of lithiation of RuO_2 is clearly monitored through the change in intensity of the Ru–Ru correlations. The subsequent two-phase conversion reaction $LiRuO_2 + 3Li^+ + 3e^- = 2Li_2O + Ru$ in stage II is clearly indicated by the isobestic point in the XANES patterns and the intensity decrease of the $LiRuO_2$-related peaks and simultaneous increase of the Ru metal peaks. In stage III, no obvious changes are seen by XANES and only minor changes by EXAFS, the latter being ascribed to the conversion of residual $LiRuO_2$ at the beginning of this stage. Again this indicates that the main contribution to the additional capacity generated here

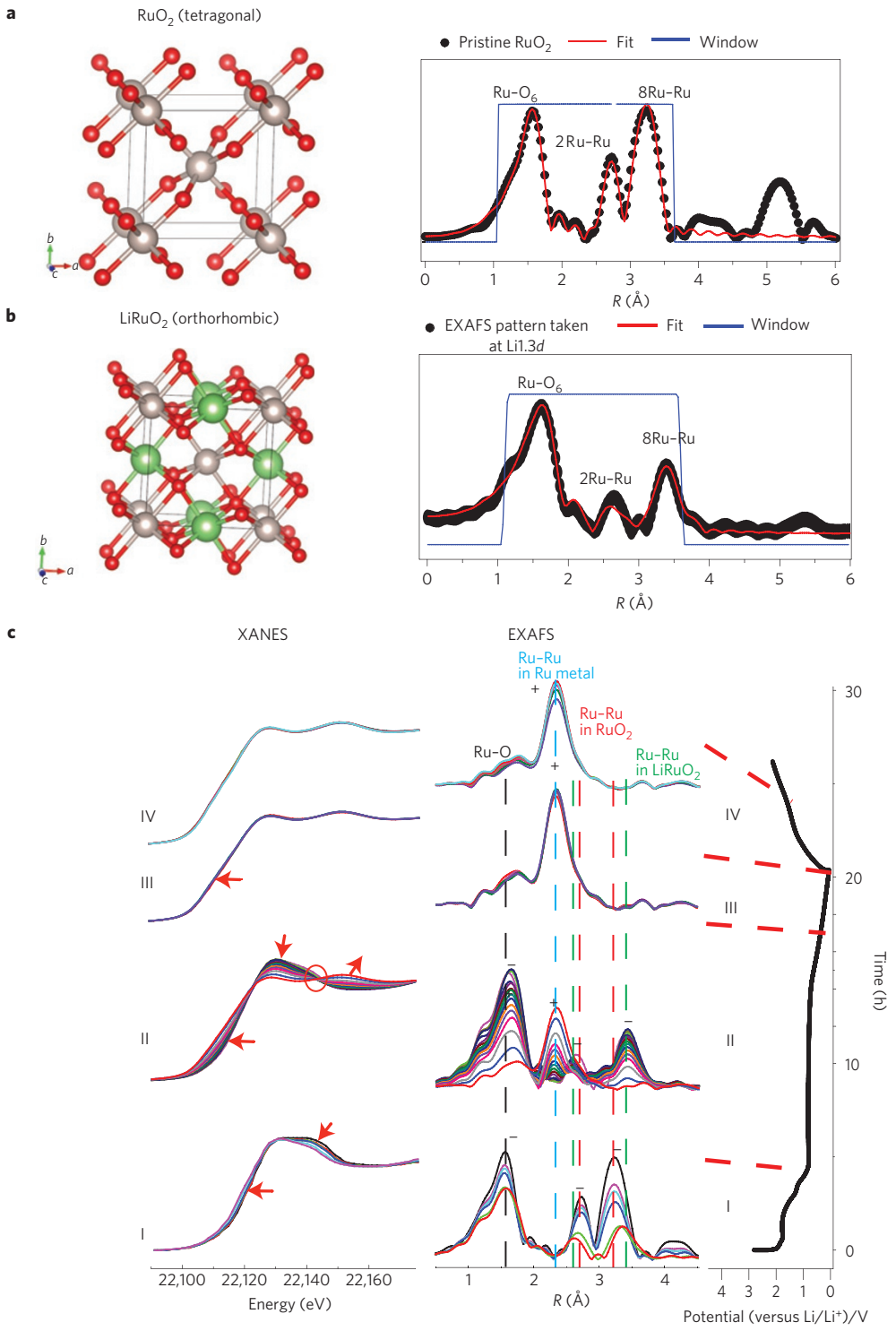

Figure 2 | *In situ* XAS analyses of the RuO_2/Li system reveal the changes in the average oxidation state of ruthenium, phase composition and bond lengths. The full capacity of the RuO_2/Li battery is accessed over 20 h (rate: *C*/20). **a**,**b**, The extended EXAFS pattern of pristine RuO_2 (rutile; **a**) and the pattern taken at Li1.3*d* (**b**) were first modelled so as to track the structural changes using the *in situ* EXAFS patterns. The observed lengthening of the Ru–O bond lengths from 1.95 and 2.00 Å (RuO_2) to 2.02 and 2.10 Å ($LiRuO_2$) is consistent with the PDF analysis. **c**, The electrochemistry profile of the discharge process/beginning of charge and the corresponding *in situ* XANES and EXAFS patterns, divided into four stages on discharge (I–III) and on charge (IV). + and − are used to indicate whether the peaks increase or decrease in intensity during the different stages.

does not involve a redox reaction of Ru-containing phases. At the initial stage of battery charging (stage IV), no pronounced changes in XANES and EXAFS are observed, except a small increase in the amplitude of the Ru peaks in EXAFS, possibly a sign of slight growth in particle size.

Identifying the sources of the 'additional capacity' by NMR spectroscopy. Although *in situ* and *ex situ* X-ray techniques reveal critical information on the evolution of the Ru-containing phases during the battery cycling, they provide little information on the Li-containing Ru-free phases, and in particular, the nature of

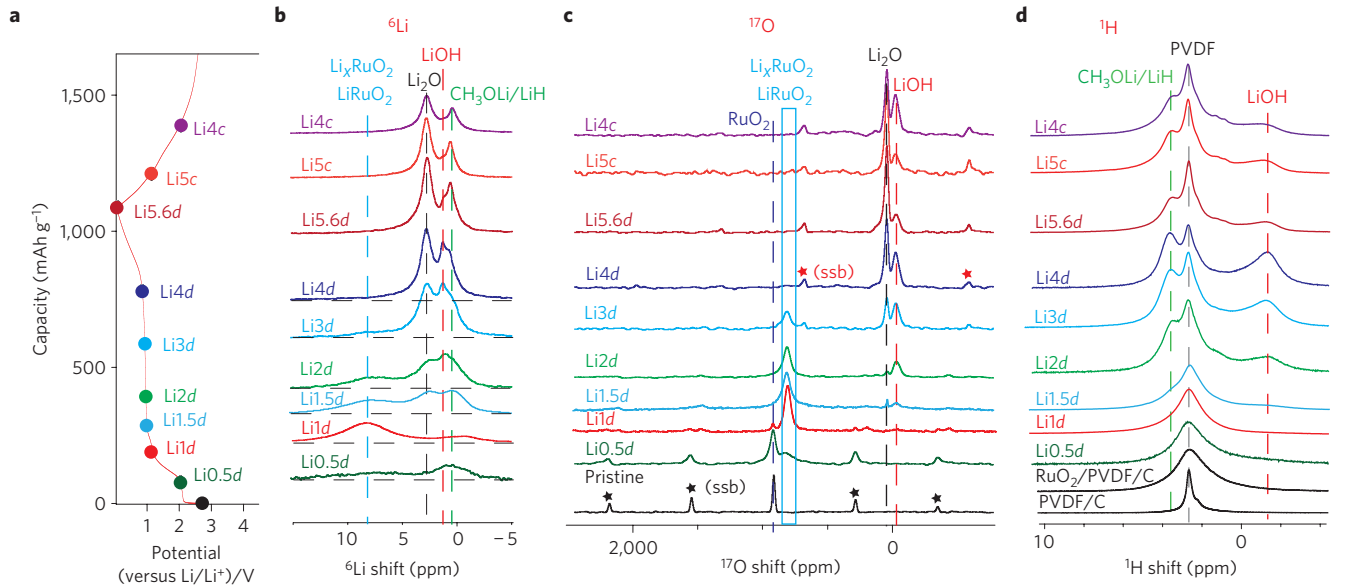

Figure 3 | Tracking the evolution of different chemical species at different states of charge in the RuO_2/Li battery system. a, The electrochemistry profile of RuO_2/Li cycled at a rate of $C/48$. **b**–**d**, *Ex situ* ^{6}Li, ^{17}O and ^{1}H NMR spectra of DMC-washed samples cycled to various states of charge as marked on the electrochemistry profile. Dashed lines marking the baselines are shown for the first few spectra in the ^{6}Li series in **b** to assist in the observation of the broad $LiRuO_2$ peak at ~8 ppm. Asterisks in **c** indicate spinning side bands.

the electrochemical process near the end of discharge, and in Stage II, both of which seem to be associated with the additional capacity generated in this metal oxide system. Different from X-ray-based techniques, solid-state NMR is an excellent tool for studying light elements such as H, Li and O, and for characterizing amorphous/nanosized phases. Various points are sampled along the discharge curve and at the beginning of the charge process (Fig. 3a) for one-dimensional high-resolution ^{6}Li, ^{17}O and ^{1}H magic-angle spinning solid-state NMR characterization (Fig. 3 and Supplementary Information). Focusing initially on stages I–II, insertion of Li into the rutile RuO_2 structure (stage I) gives rise to a broad ^{6}Li resonance at ~8 ppm due to the lithiated ruthenate phases[22] (Fig. 3b). (Distinct ^{6}Li resonances from the intermediate phase, Li_xRuO_2 and $LiRuO_2$ are not observed owing to the limited resolution caused by spectral broadening and the narrow Li spectral range.) This reaction is also accompanied by a signal assigned with lithium-containing SEI salts (0 ppm), such as LiF and CH_3OLi, which are formed even in this relatively high voltage window[23]. Both these phases are clearly identified by using double resonance ^{1}H–^{6,7}Li and ^{19}F–^{6,7}Li cross-polarization experiments as outlined in the Supplementary Information. The SEI grows on Li_xRuO_2/$LiRuO_2$, as indicated by the cross-peaks between the Li_xRuO_2/$LiRuO_2$ and SEI peaks in the two-dimensional (2D) ^{7}Li–^{7}Li spin exchange experiment (Supplementary Fig. 10): this 2D experiment is sensitive to the distance between different components and provides direct evidence for spatial connectivity (in the Angstrom to nanoscale). The peak intensity of Li_xRuO_2/$LiRuO_2$ grows as more lithium intercalates and reaches a maximum when more than 1 Li ion per RuO_2 formula unit is consumed (see Supplementary Table 1 for full quantification of all the ^{6}Li environments), the reaction with additional Li (~0.3 Li) arising from the parallel SEI formation process. LiOH (~1 ppm) starts to emerge at this point and the SEI continues to grow, the LiOH concentration increasing steadily up to the end of the second plateau (~Li4*d*). Li_2O (2.6 ppm; ref. 22) is observed in the spectrum of Li1.5*d*, as expected, arising from the conversion reaction, $LiRuO_2 + 3Li^+ + 3e^- = 2Li_2O + Ru$, but it does not start to grow significantly in concentration until after the insertion of 2Li.

The corresponding series of ^{17}O NMR spectra in Fig. 3c shows a similar trend. The ^{17}O NMR spectra exhibit better resolution than the ^{6}Li spectra owing to the larger ^{17}O shift range (from approximately 0–1,000 ppm) and an unambiguous assignment of LiOH and Li_2O is possible[24,25]. Furthermore, as the pristine material, $Ru^{17}O_2$, is the only component that is isotopically enriched with ^{17}O, the method allows the fate of the oxygen in the RuO_2 particles to be tracked. The initial insertion of lithium into RuO_2 (^{17}O resonance at 917 ppm) results in a broad resonance at 820 ppm assigned to Li_xRuO_2. The breath of this resonance is ascribed to a distribution of local environments. The resonance shifts to 807 ppm and sharpens (Li1*d*) as the lithiation process proceeds with the transformation from Li_xRuO_2 to $LiRuO_2$, consistent with the PDF and EXAFS analyses. Li^{17}OH (−22 ppm, assignment confirmed in Supplementary Fig. 6)[24] is clearly observed along with the conversion reaction to form $Li_2{}^{17}O$, consistent with the ^{6}Li NMR spectra. From Li2*d* to Li4*d*, the conversion from $LiRuO_2$ (807 ppm) to Li_2O and Ru is manifested by the gradual decrease to almost zero of the $LiRuO_2$ peak intensity and a noticeable increase of the Li_2O peak (38 ppm) intensity.

The ^{1}H spectrum (Fig. 3d) of the pristine RuO_2 cathode film (comprising RuO_2, Super P carbon and polyvinylidene fluoride (PVDF) copolymer) shows a very broad peak centred at 2.6 ppm, largely due to the CH_2 group of PVDF copolymer. However, when compared with the ^{1}H spectrum of PVDF mixed with only Super P carbon, the ^{1}H spectrum of pristine RuO_2 cathode film is much broader and the broad component is tentatively ascribed to surface –OH groups on the RuO_2 nanoparticles[26,27], which will exist in heterogeneous environments and probably show a broad chemical shift distribution. Little change in the ^{1}H spectrum is seen until CH_3OLi (a product from the decomposition of the electrolyte solvent dimethyl carbonate[28] (DMC)), is observed (at Li1.5*d*) at ~3.5 ppm. The ^{1}H–^{7}Li correlation NMR spectra in Supplementary Fig. 5a,b confirm this assignment. A ^{1}H resonance from LiOH at −1.3 ppm is clearly seen at Li2*d*, increasing in intensity from Li2*d* to Li4*d* consistent with the ^{6}Li and ^{17}O NMR. Again, the ^{1}H–^{7}Li correlation spectra (Supplementary Fig. 5) confirm the assignment of the −1.3 ppm ^{1}H and 1 ppm ^{6}Li/^{7}Li resonances to LiOH.

After the insertion of 4 Li, the gradual decrease in discharge voltage (stage III) is associated with the continuous decrease in the

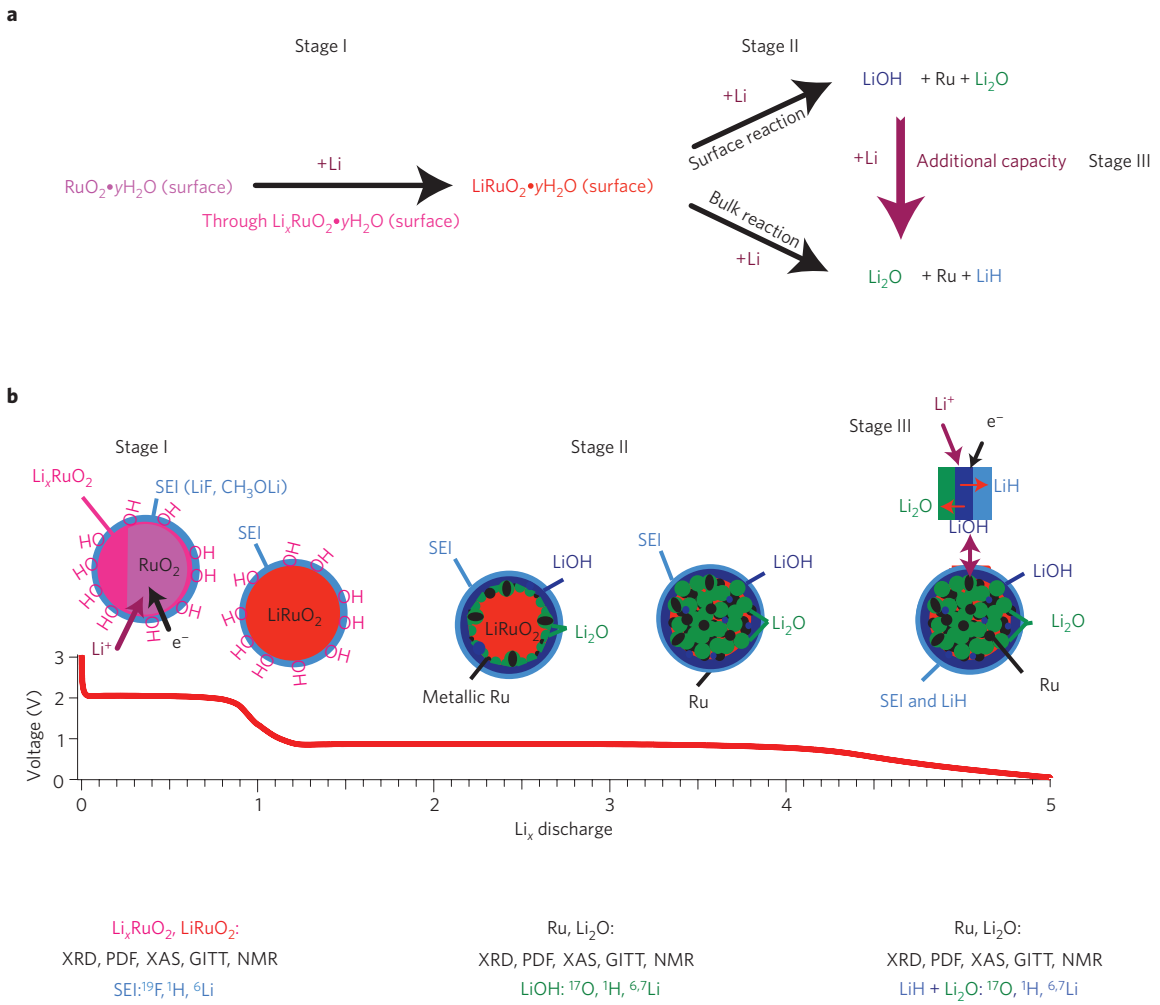

Figure 4 | Summary of the reaction pathway, evolution of phase distribution and relevant experimental evidence of the RuO_2/Li battery system. **a**, Summarized reaction pathway. **b**, The profile of the electrochemistry with schematics representing the phase distribution at each stage of discharge. The relevant supporting evidence is given below. GITT, galvanostatic intermittent titration technique.

amount of LiOH, whereas the intensities of ^{6}Li and ^{17}O NMR peaks of Li_2O and the ^{6}Li resonance of SEI (~0 ppm) increase noticeably (^{6}Li and ^{17}O NMR). By carefully comparing the ^{1}H–^{7}Li correlation NMR spectra of sample Li5.6*d* with those of a LiH standard sample (Supplementary Figs 4 and 5) it is clear that the ~0 ppm ^{7}Li/^{6}Li resonances in Li5.6*d* result from not only CH_3OLi but also LiH (see Supplementary Fig. 5). From Li4*d* to Li5.6*d*, the increase in the intensity of the ~0 ppm ^{6}Li peak (Fig. 3b) is largely due to the formation of LiH not CH_3OLi. LiH formation is accompanied by a significant decrease in the intensity of the LiOH peaks in the ^{6}Li (1 ppm), ^{17}O (−22 ppm) and ^{1}H (−1.3 ppm) spectra from Li4*d* to Li5.6*d*. Thus, a major reaction that contributes to the additional capacity in the Li/RuO_2 system involves the conversion reaction of $LiOH + 2Li^+ + 2e^- = Li_2O + LiH$. On charging the battery, the amount of LiOH increases again, which indicates that the above reaction, $LiOH + 2Li^+ + 2e^- = Li_2O + LiH$, is at least partially reversible.

Two-dimensional ^{6}Li–^{6}Li and ^{1}H–^{1}H exchange NMR experiments (Supplementary Fig. 11) reveal that LiOH, CH_3OLi/LiH and Li_2O are spatially close to one another on the nanoscale and at least some LiOH is located between CH_3OLi/LiH and bulk Li_2O, consistent with the proposal that LiH is formed from the LiOH.

To provide further evidence for the LiOH ⟨−⟩ LiH reaction, a LiOH/Li cell was prepared and cycled (Supplementary Fig. 9). Although the first approximately 125 mAh g^{-1} of capacity (between 1.5 and 0.3 V) can be ascribed primarily to SEI formation on the carbon in the carbon/LiOH composite electrode, an additional 400 mAh g^{-1} of capacity is observed between 0.25 and 0V. The ^{6}Li and ^{1}H NMR spectra collected at various stages of discharge are similar to those seen in the RuO_2/Li system, and confirm that conversion of LiOH to form Li_2O and LiH has occurred. First-principles calculations predict an open-circuit voltage (OCV) of 0.89 V for this reaction, similar to the value obtained from the standard enthalpies of the reactants and products of ~1.04 V.

First-principles calculations have been carried out to examine the possibility that the extra capacity is generated owing to a 'space charge' effect between Ru and Li_2O, as proposed before[12,14,15]. Our calculations show that the inserted Li atoms between the Li_2O and Ru phases prefer to adsorb on the Ru surface rather than on the Li_2O surface when the Li_2O and Ru phases are well separated. When the Li_2O phase approaches the Ru surface (forming a 'grain boundary'), the calculated OCV barely changes, and we found no evidence for a synergistic effect between Ru and Li_2O on the energetics associated with additional Li storage at the interfaces (see Supplementary Fig. 14), albeit for the limited choice of surfaces that we investigated. The formation of up to a monolayer coverage of Li on the surface of the Ru metal nanoparticles is, however, energetically feasible and is associated with an OCV of 0.5–1 V; this may account for at least a part of the Li uptake in previous electrochemical experiments where a capacity of ~0.17 lithium per Ru was found when using electrodes containing 10–20 nm Ru

nanoparticles[27]. This mechanism is different from the capacitive process ruled out by the experiments reported in ref. 16.

In conclusion, a multi-faceted investigation has been carried out to identify major sources of the additional capacity observed in the RuO_2/Li cell, and the combined results are schematically illustrated in Fig. 4. The process starts with (tetragonal) RuO_2 rutile particles (with some OH groups present on the external and internal surfaces of RuO_2, written as $RuO_2 \cdot yH_2O$) of ~100 nm in size. Lithium insertion occurs to form the orthorhombic $LiRuO_2$ phase through the intermediate (tetragonal) Li_xRuO_2 phase. LiOH is observed, which is accompanied by the onset of the conversion reaction to form Ru metal and Li_2O. LiOH formation must largely involve the surface OH groups (rather than the electrolyte oxygen atoms) because the formed product is enriched in ^{17}O. The protons are either present on the original RuO_2 particles or are formed from electrolyte decomposition. Note that although not all systems will contain as many protons as the RuO_2 system, the decomposition of the electrolyte, catalysed by the metallic nanoparticles generated in conversion reactions, is quite general[23]. The conversion reaction continues to form ~1.3 nm Ru metal nanoparticles and Li_2O at a voltage of ~0.8 V; below 0.8 V, the conversion reaction of LiOH to form Li_2O and LiH takes place. SEI (LiF dominating at high voltages and CH_3OLi at lower voltages) formation is also observed throughout the discharge process by NMR. Although the formation of LiOH and its subsequent reversible conversion to Li_2O and LiH is identified as a major source of the additional capacity generation in this system, other mechanisms can also lead to minor contributions, for instance, reversible SEI formation[10] and simple Li adsorption on the surface of Ru nanoparticles[27] (as investigated in the calculations).

Finally, this article illustrates an effective NMR protocol for investigating the nature of many phases present in the amorphous SEI, and their spatial proximities within the composite electrode. This methodology will be relevant to the study of many battery systems; the nature of the SEI and electrolyte decomposition having been shown to be critical to the performance of several highly promising electrode systems, such as Si-anode-based and lithium–air batteries.

Methods

Materials. RuO_2 was purchased from Sigma-Aldrich and enriched with $^{17}O_2$ gas. ^{17}O-enrichment of the pristine RuO_2 was carried out by heating the RuO_2 power in a saturated $^{17}O_2$ gas atmosphere at 800 °C overnight and followed by cooling down to room temperature gradually. High-energy ball-milling was applied for 30-min to reduce the particle size of RuO_2 to below 100 nm. Then RuO_2 powder was mixed with Super P Li (Timcal) and Flex 2801 Kynar PVDF in a weight ratio of RuO_2/PVDF/Super P = 9.33:2.48:1 (72.84 wt% of RuO_2). Acetone and dibutyl phthalate were added to the mixture to form self-supporting cathode film. Dibutyl phthalate was removed by soaking the electrodes in anhydrous ether. The cathode film was dried under vacuum overnight before being used to make RuO_2/Li batteries. Following cycling, the battery cells were rested for more than 10 h before recovering the active material for the *ex situ* NMR studies. The retrieved material was first washed twice with 3 ml anhydrous DMC and then soaked in 3 ml anhydrous DMC overnight. The solvent was decanted and the wet active material was dried overnight under dynamic vacuum at room temperature. NMR spectra were also collected for some cells without washing the electrodes.

X-ray diffraction/PDF and XAS characterization. The high-energy total scattering measurements were performed with self-supporting RuO_2 electrodes assembled into the 'AMPIX' electrochemical cell[29]. Cells were cycled galvanostatically against lithium at a constant current of 37 mA g^{-1} ($C/30$), in the range 3.5 V–0.05 V. High-energy total X-ray scattering data ($\lambda = 0.2128$ Å) were collected at the dedicated PDF beamline 11-ID-B at the Advanced Photon Source, Argonne National Laboratory. A large-area amorphous-silicon-based detector (Perkin-Elmer) was used to collect data to high values of momentum transfer ($Q_{max} \sim 18$ $Å^{-1}$; ref. 30). Data were collected at 30 min intervals using 3 min exposures. The raw images were integrated using the software FIT2d (ref. 31). PDFgetX2 (ref. 32) was used to correct the data for background contributions, Compton scattering and detector effects, and to Fourier transform the data to generate $G(r)$, the PDF. Structure models were refined against the PDF data within PDFgui (ref. 33). The intensity and position of peaks corresponding to the Ru–O and Ru–Ru bonds in these phases were quantified by fitting Gaussian functions to features in the PDFs within Fityk[34].

A standard 2032 coin cell with a small hole at both sides was used for the *in situ* XAS measurements. Glassy carbon was used as the current collector underneath the electrode to improve the homogeneity of the reaction across the whole battery cell. *In situ* Ru K-edge XAS spectra were collected in transmission mode at beamlines X18A and X18B at the National Synchrotron Light Source of Brookhaven National Laboratory using a Si(111) double-crystal monochromator. The *in situ* XAS spectra were continuously collected during lithiation with a $C/20$ rate. Reference spectra of a metallic Ru foil were simultaneously collected with the corresponding *in situ* spectra for energy calibration. Details of the data processing and refinement protocol can be found in the Supplementary Information.

NMR characterization. Solid-state NMR measurements (^1H, ^6Li and ^{17}O) were performed in a 16.4 T magnetic field with a Bruker Avance III spectrometer and a 1.3 mm probe-head at a magic-angle spinning speed of 60 kHz. The $\pi/2$ pulse lengths were 2.5 µs for ^1H, 2.6 µs for ^6Li, and 0.65 µs (solid $\pi/2$) for ^{17}O. The chemical shifts of ^1H, ^6Li and ^{17}O were calibrated by using adamantane (^1H at 1.87 and 1.75 ppm), 1 M ^6LiCl solution at room temperature (0 ppm) and cubic $Ce^{17}O_2$ (877 ppm), respectively. The ^1H spectra were normalized by using the ^1H peak from PVDF (2.6 ppm) as an internal standard. The ^6Li, ^{17}O and ^1H spectra have been collected consecutively for each sample; thus the scaling factors used in the ^1H spectra normalization are adopted to normalize the ^6Li and ^{17}O spectra. The normalization of the ^6Li and ^{17}O spectra was cross-checked by measuring the total integral of each spectrum, where the total ^6Li signal was confirmed to be close to the Li amount calculated on the basis of the electrochemistry (the total current passed) and ^{17}O signal should remain approximately constant because there should be no or little ^{17}O loss/gain during the electrochemical processes.

First-principles calculations. All of the theoretical calculations were performed using density functional theory within the plane-wave pseudopotential framework as implemented in the Quantum ESPRESSO code[35]. The Perdew–Burke–Ernzerhof[36] exchange–correlation functional was employed. The core electrons were replaced by ultrasoft pseudopotentials[37], and the valence electrons were expanded by plane-wave basis sets with kinetic energy cutoffs of 25 Ry and 250 Ry for wavefunction and charge density, respectively. Detailed descriptions of the models and the method used to calculate the OCVs can be found in the Supplementary Information.

Received 3 April 2013; accepted 16 September 2013; published online 3 November 2013

References

1. Idota, Y., Kubota, T., Matsufuji, A., Maekawa, Y. & Miyasaka, T. Tin-based amorphous oxide: A high-capacity lithium-ion-storage material. *Science* **276,** 1395–1397 (1997).
2. Poizot, P., Laruelle, S., Grugeon, S., Dupont, L. & Tarascon, J. M. Nano-sized transition-metal oxides as negative-electrode materials for lithium-ion batteries. *Nature* **407,** 496–499 (2000).
3. Amatucci, G. G. & Pereira, N. Fluoride based electrode materials for advanced energy storage devices. *J. Fluor. Chem.* **128,** 243–262 (2007).
4. Balaya, P., Li, H., Kienle, L. & Maier, J. Fully reversible homogeneous and heterogeneous Li storage in RuO_2 with high capacity. *Adv. Funct. Mater.* **13,** 621–625 (2003).
5. Badway, F., Cosandey, F., Pereira, N. & Amatucci, G. G. Carbon metal fluoride nanocomposites—high-capacity reversible metal fluoride conversion materials as rechargeable positive electrodes for Li batteries. *J. Electrochem. Soc.* **150,** A1318–A1327 (2003).
6. Li, H., Balaya, P. & Maier, J. Li-storage via heterogeneous reaction in selected binary metal fluorides and oxides. *J. Electrochem. Soc.* **151,** A1878–A1885 (2004).
7. Li, H., Richter, G. & Maier, J. Reversible formation and decomposition of LiF clusters using transition metal fluorides as precursors and their application in rechargeable Li batteries. *Adv. Mater.* **15,** 736–739 (2003).
8. Liao, P., MacDonald, B. L., Dunlap, R. A. & Dahn, J. R. Combinatorially prepared [LiF](1-*x*)Fe-*x* nanocomposites for positive electrode materials in Li-ion batteries. *Chem. Mater.* **20,** 454–461 (2008).
9. Cabana, J., Monconduit, L., Larcher, D. & Palacin, M. R. Beyond intercalation-based Li-ion batteries: The state of the art and challenges of electrode materials reacting through conversion reactions. *Adv. Mater.* **22,** E170–E192 (2010).
10. Beaulieu, L. Y., Larcher, D., Dunlap, R. A. & Dahn, J. R. Reaction of Li with grain-boundary atoms in nanostructured compounds. *J. Electrochem. Soc.* **147,** 3206–3212 (2000).
11. Laruelle, S. *et al.* On the origin of the extra electrochemical capacity displayed by MO/Li cells at low potential. *J. Electrochem. Soc.* **149,** A627–A634 (2002).

12. Jamnik, J. & Maier, J. Nanocrystallinity effects in lithium battery materials—Aspects of nano-ionics. Part IV. *Phys. Chem. Chem. Phys.* **5,** 5215–5220 (2003).
13. Maier, J. Mass storage in space charge regions of nano-sized systems (Nano-ionics. Part V). *Faraday Discuss.* **134,** 51–66 (2007).
14. Zhukovskii, Y. F., Balaya, P., Kotomin, E. A. & Maier, J. Evidence for interfacial-storage anomaly in nanocomposites for lithium batteries from first-principles simulations. *Phys. Rev. Lett.* **96,** 058302 (2006).
15. Zhukovskii, Y. F., Balaya, P., Dolle, M., Kotomin, E. A. & Maier, J. Enhanced lithium storage and chemical diffusion in metal-LiF nanocomposites: Experimental and theoretical results. *Phys. Rev. B* **76,** 235414 (2007).
16. Ponrouch, A., Taberna, P. L., Simon, P. & Palacin, M. R. On the origin of the extra capacity at low potential in materials for Li batteries reacting through conversion reaction. *Electrochim. Acta* **61,** 13–18 (2012).
17. Menkin, S., Golodnitsky, D. & Peled, E. Artificial solid–electrolyte interphase (SEI) for improved cycleability and safety of lithium-ion cells for EV applications. *Electrochem. Commun.* **11,** 1789–1791 (2009).
18. Peled, E., Golodnitsky, D., Ulus, A. & Yufit, V. Effect of carbon substrate on SEI composition and morphology. *Electrochim. Acta* **50,** 391–395 (2004).
19. Eshkenazi, V., Peled, E., Burstein, L. & Golodnitsky, D. XPS analysis of the SEI formed on carbonaceous materials. *Solid State Ion.* **170,** 83–91 (2004).
20. Ohzuku, T., Sawai, K. & Hirai, T. Topotactic 2-phase reaction of ruthenium dioxide (rutile) in lithium nonaqueous cell. *J. Electrochem. Soc.* **137,** 3004–3010 (1990).
21. Munoz-Rojas, D., Casas-Cabanas, M. & Baudrin, E. Effect of particle size and cell parameter mismatch on the lithium insertion/deinsertion processes into RuO_2. *Solid State Ion.* **181,** 536–544 (2010).
22. Bekaert, E., Balaya, P., Murugavel, S., Maier, J. & Menetrier, M. Li-6 MAS NMR investigation of electrochemical lithiation of RuO_2: Evidence for an interfacial storage mechanism. *Chem. Mater.* **21,** 856–861 (2009).
23. Gmitter, A. J. *et al.* Formation, dynamics, and implication of solid electrolyte interphase in high voltage reversible conversion fluoride nanocomposites. *J. Mater. Chem.* **20,** 4149–4161 (2010).
24. Leskes, M. *et al.* Direct detection of discharge products in lithium–oxygen batteries by solid-state NMR spectroscopy. *Angew. Chem. Int. Ed.* **51,** 8560–8563 (2012).
25. Mackenzie, K.J.D., Smith, & M. E., *Multinuclear Solid-State NMR of Inorganic Materials* Ch. 6 (Pergamon, 2002).
26. Ma, Z. R., Zheng, J. P. & Fu, R. Q. Solid state NMR investigation of hydrous ruthenium oxide. *Chem. Phys. Lett.* **331,** 64–70 (2000).
27. Delmer, O. *Size and morphology effects on the cell voltage of Li-batteries: Case Study of* RuO_2. PhD thesis, Max Planck Institute, (2009).
28. Zhuang, G. V., Yang, H., Ross, P. N., Xu, K. & Jow, T. R. Lithium methyl carbonate as a reaction product of metallic lithium and dimethyl carbonate. *Electrochem. Solid State* **9,** A64–A68 (2006).
29. Borkiewicz, O. J. *et al.* The AMPIX electrochemical cell: A versatile apparatus for in situ X-ray scattering and spectroscopic measurements. *J. Appl. Crystallogr.* **45,** 1261–1269 (2012).
30. Chupas, P. J. *et al.* Rapid-acquisition pair distribution function (RA-PDF) analysis. *J. Appl. Crystallogr.* **36,** 1342–1347 (2003).
31. Hammersley, A. P., Svensson, S. O., Hanfland, M., Fitch, A. N. & Hausermann, D. Two-dimensional detector software: From real detector to idealised image or two-theta scan. *High Press. Res.* **14,** 235–248 (1996).
32. Qui, X., Thompson, J. W. & Billinge, S. J. L. PDFgetX2: A GUI driven program to obtain the pair distribution function from X-ray powder diffraction data. *J. Appl. Crystalogr.* **37,** 678 (2004).
33. Farrow, C. L. *et al.* PDFfit2 and PDFgui: Computer programs for studying nanostructure in crystals. *J. Phys. Condens. Mater.* **19,** 335219 (2007).
34. Wojdyr, M. Fityk: A general-purpose peak fitting program. *J. Appl. Crystallogr.* **43,** 1126–1128 (2010).
35. Giannozzi, P. *et al.* QUANTUM ESPRESSO: A modular and open-source software project for quantum simulations of materials. *J. Phys. Condens. Mater.* **21** (2009).
36. Perdew, J. P., Burke, K. & Ernzerhof, M. Generalized gradient approximation made simple. *Phys. Rev. Lett.* **77,** 3865–3868 (1996).
37. Vanderbilt, D. Soft self-consistent pseudopotentials in a generalized eigenvalue formalism. *Phys. Rev. B* **41,** 7892–7895 (1990).

Acknowledgements

This research was supported as part of the North Eastern Center for Chemical Energy Storage, an Energy Frontier Research Center funded by the US Department of Energy, Office of Science, and Office of Basic Energy Sciences under Award Number DE-SC0001294. Work done at Argonne and use of the Advanced Photon Source, an Office of Science User Facility operated for the US Department of Energy (DOE) Office of Science by Argonne National Laboratory, was supported by the US DOE under Contract No. DE-AC02-06CH11357. Use of the National Synchrotron Light Source, Brookhaven National Laboratory, was supported by the US DOE, Office of Science, Office of Basic Energy Sciences, under Contract No. DE-AC02-98CH10886. Y-Y.H. acknowledges support from a Newton International Fellowship from the Royal Society and a Marie Curie International Incoming Fellowship (PIIF-GA-2011_299341). We thank A. Van der Ven (University of Michigan) and M. Leskes (University of Cambridge) for constructive discussions.

Author contributions

C.P.G. and Y-Y.H. proposed the concepts and designed the experiments. Y-Y.H., Z.L., K-W.N., O.J.B., X.H., J.C., K.M.W., L-S.D. and X.Y. carried out the experiments, C.P.G., Y-Y.H., K-W.N., O.J.B., X.H., J.C., M.T.D., K.W.C., P.J.C., X.Y. and X-Q.Y. performed the analysis. C.P.G. and Y-Y.H. wrote the manuscript with help from all the co-authors.

Additional information

Supplementary information is available in the online version of the paper. Reprints and permissions information is available online at www.nature.com/reprints. Correspondence and requests for materials should be addressed to C.P.G.

Competing financial interests

The authors declare no competing financial interests.